Energy Storage Materials 21 (2019) 210–218

Contents lists available at ScienceDirect

Energy Storage Materials

journal homepage: www.elsevier.com/locate/ensm

Cobalt nitride nanoparticles embedded in porous carbon nanosheet arrays propelling polysulfides conversion for highly stable lithium–sulfur batteries

Han Zhang[a,1], Dongxu Tian[b,1], Zongbin Zhao[a,*], Xuguang Liu[c], Ya-Nan Hou[a], Yujiao Tang[b], Jingjing Liang[a], Zhichao Zhang[b], Xuzhen Wang[a,b], Jieshan Qiu[a,*]

[a] State Key Lab of Fine Chemicals, Liaoning Key Lab for Energy Materials and Chemical Engineering, PSU-DUT Joint Center for Energy Research, Environmental and Biological Science and Technology, Dalian University of Technology, Dalian 116024, China
[b] School of Chemistry, Dalian University of Technology, Dalian 116024, China
[c] Key Lab of Interface Science and Engineering in Advanced Materials, Ministry of Education, Taiyuan University of Technology, Taiyuan 030024, China

ARTICLE INFO

Keywords:
Lithium-sulfur batteries
Cobalt nitride
Polysulfide adsorption
Catalytic effect

ABSTRACT

Compared with currently mature lithium ion batteries, lithium-sulfur batteries (LSBs) show many remarkable advantages for next-generation electrical energy storage owing to high theoretical specific energy and low cost. However, the shuttle effect, low conductivity of sulfur cathode, and sluggish kinetics are remarkable barriers preventing their realistic application. Herein, we present a facile strategy in which cobalt nitride (Co_4N) nanoparticles embedded leaf-like porous carbon nanosheet arrays are grown on flexible carbon cloth as a free-standing cathode for high-performance LSBs. Co_4N not only adsorbs the intermediate lithium polysulfides (LiPSs) strongly, but also catalytically promotes the mutual transformation between sulfur and Li_2S. Moreover, theoretical simulations reveal the strong interaction between Co_4N and sulfur species. The created free-standing cathode exhibits a high capacity of 1121 mAh g^{-1} after 100 cycles at 0.5 C, a high rate performance (746 mAh g^{-1} at a high rate of 5 C relative to 1237 mAh g^{-1} at 0.2 C), and high stable cycle performance (598 mAh g^{-1} at 5 C over 500 cycles with ultralow 0.035% decay per cycle). Our method provides a new potential avenue for energy conversion and storage devices based on multi-electron redox reactions.

1. Introduction

With the rapid developments in electric automobile and portable electronic devices, lithium-sulfur batteries (LSBs) show higher theoretical specific capacity (1675 mAh g^{-1}) and energy density (2600 Wh kg^{-1}), compared with currently developed alkali (Li, Na, K) ion battery [1]. Moreover, high abundance and nontoxicity of sulfur and rather low price make lithium-sulfur batteries more appealing. However, LSBs are still facing huge obstacles for real application because of their serious polysulfides dissolution and poor electrical conductivity of sulfur [2–4]. To tackle these issues, various novel host materials have been developed for LSBs cathode to confine the polysulfides. Along this line, a variety of different carbon-based materials, such as carbon nanofibers [5,6], carbon nanotubes [7,8], graphene [9–11] and carbon nanospheres [12] have been integrated into composite materials with sulfur. All these carbonaceous host materials on the cathode greatly enhance the conductivity of materials, and eventually improve the performance of the batteries. Furthermore, rational design of carbon-based nanostructures has been widely investigated for polysulfide trapping [13,14]. Nevertheless, the weak interaction between nonpolar carbon and polar LiPSs limits the capture ability, recycling efficiency and long-term cycling stability [15].

The shuttle effect is primarily derived from the following two reasons. One is the soluble LiPSs dissolution into electrolyte and the other is the slow kinetics of cell reaction [16]. Generally, to obtain the high performance of LSBs, the contact between sulfur and electrolyte is necessary and resulting from unavoidable dissolution of LiPSs. Therefore, the most effective way to restrain the shuttling is to promote the mutual transformation between sulfur and Li_2S [17]. Recently, some sulfides (CoS_2 [18], MoS_2 [19]), oxides (Fe_2O_3 [20], V_2O_5 [21]), nitrides (VN [22]) and perovskite [23] are found to be able to form strong chemical bonds with LiPSs, as well as catalytically promote the conversion of LiPSs to Li_2S_2/Li_2S, indicating a rational way for the construction of LSBs' electrode materials.

Compared with the other materials, transition metal nitrides have drawn enormous attention as a result of their good chemical stability [24,25], high conductivity [26] and high catalytic activity [27,28]. Typically, as a potential electrode material, cobalt nitride (Co_4N) offers

* Corresponding authors.
E-mail addresses: zbzhao@dlut.edu.cn (Z. Zhao), jqiu@dlut.edu.cn (J. Qiu).
[1] H. Zhang and D.-X. Tian contributed equally to this work.

https://doi.org/10.1016/j.ensm.2018.12.005
Received 28 September 2018; Received in revised form 20 November 2018; Accepted 4 December 2018
Available online 05 December 2018

the following advantages: (i) high electrical conductivity (1.67×10^5 S m^{-1} at room temperature) [27] that facilitates rapid ion and electron transformation on active material surface. (ii) effective inhibition of the shuttle effect by strong chemical adsorption for polysulfides [29]. (iii) the catalytic behavior that promotes the mutual transformation between sulfur and Li_2S.

Herein, we design a facile way for fabricating the free-standing carbon cloth based materials grown with vertical zeolite imidazole frameworks (ZIFs) derived porous carbon nanosheet arrays embedded by Co_4N nanoparticles (note as CC@Co_4N-PCNA). The CC@Co_4N-PCNA nanohybrids, featured with three-dimensional (3D) interconnected network, facilitate the transportation of lithium ions and electrons, and the Co_4N nanoparticles not only show strong chemical adsorption for LiPSs but also catalytically promote the mutual transformation between sulfur and Li_2S. As a free-standing cathode material, the S/CC@Co_4N-PCNA composites exhibit a high capacity of 1121 mAh g^{-1} after 100 cycles at 0.5 C, a high rate capability (1356 and 746 mAh g^{-1} are achieved at discharge/charge rates at 0.2 C and 5 C, respectively), an ultralow capacity fade rate of 0.035% per cycle over 500 cycles at 5 C with outstanding Coulombic efficiency ≈ 100%.

2. Experimental

2.1. Preparation of CC@ZIF-67

Carbon cloths (CC 2 cm × 2 cm) were treated by HNO_3 (69%) at 90°C for 6 h and washed with deionized water, ethanol and acetone for several times to remove excess acid, then immersed in deionized water (100 mL) containing $Co(NO_3)_2{\cdot}6H_2O$ (0.72 g) and 2-methylimidazole (2-MeIm, 1.64 g) without disturbance. After 4 h of reaction at room temperature (RT), the CC@ZIF-67 was washed with water and ethanol for several times and dried at 60 °C overnight.

2.2. Preparation of CC@Co_3O_4-PCNA and CC@Co_4N-PCNA

Typically, a piece of CC@ZIF-67 was mounted into a tube furnace, heated to 600 °C at 2 °C min^{-1} and maintained for 2 h in N_2 atmosphere and then to 330 °C for 2 h in air. The furnace was then allowed to be cooled naturally to RT, and the final product was denoted as CC@Co_3O_4-PCNA. The as-prepared CC@Co_3O_4-PCNA was placed into a tube furnace. Then, the furnace was heated to 350 °C at 5 °C min^{-1} and then to 600 °C at 2 °C min^{-1}, kept at this final temperature for 3 h under a flowing NH_3 (50 sccm). The as-prepared Co_4N embedded porous carbon nanosheet arrays on carbon cloth was denoted as CC@Co_4N-PCNA.

2.3. Preparation of CC@PCNA, CC@Co_4N NWs, ZIF-67 and Co_4N-PC

The CC@ZIF-67 was annealed in a tube furnace, heated to 600 °C at 2 °C min^{-1} for 2 h at N_2 atmosphere. yielding that product was washed with a sulfuric acid solution (1 M) solution for 24 h to remove the Co metal nanoparticles and was noted as CC@PCNA.

The CC@Co_3O_4 Nanowires (CC@Co_3O_4 NWs) was synthesized using the reported method with modified procedures [24]. The CC@Co_3O_4 NWs precursor was prepared using a simple hydrothermal method. In a typical synthesis, $Co(NO_3)_2{\cdot}6H_2O$ (0.41 g), NH_4F (0.13 g) and urea (0.42 g) were dissolved into deionized water (50 mL) under vigorous stirring for 10 min, and then a piece of HNO_3-treated CC was immersed into the above solution for another 10 min. The solution and CC were transferred into a 100 mL Teflon-lined stainless-steel autoclave and maintained at 120 °C for 5 h. After the autoclave was cooled down to RT, the sample was washed with water and ethanol for several times, and dried at 60 °C for 12 h. Then the sample was heated to 330 °C and maintained for 2 h in air. The final black carbon cloth composite was denoted as CC@Co_3O_4 NWs. The CC@Co_4N NWs were prepared form CC@Co_3O_4 NWs under the same heating procedure for CC@Co_4N-PCNA.

In a typical preparation, $Co(NO_3)_2{\cdot}6H_2O$ (0.72*g*) and 2-MeIm (1.64*g*) were dissolved into deionized water (50 mL). After thorough mixing, the solution was incubated at RT for 4 h. The as-obtained precipitates were collected by centrifugation, washed with ethanol and water for 3 times and dried at 70 °C overnight. The Co_4N-PC was prepared from ZIF-67 under the same procedure for CC@Co_4N-PCNA.

2.4. Preparation of the sulfur composites

The S/CC@Co_4N-PCNA, S/CC@Co_3O_4-PCNA, S/CC@Co_4N NWs, S/CC@PCNA and S/CC composites were prepared by a melt-diffusion method [50]. To uniformly distribute sulfur in the CC@Co_4N-PCNA, sulfur (0.15 g) was dissolved into CS_2 (10 mL). Dry CC@Co_4N-PCNA composite was completely soaked into the CS_2 solution for 20 min, and then dried at 50 °C for 6 h. Then the CC@Co_4N-PCNA composite was heated at Ar atmosphere at 155 °C for 12 h (Fig. S1c). The S/CC@Co_3O_4-PCNA, S/CC@Co_4N NWs, S/CC@PCNA and S/CC composites were prepared by the same general procedure. The sulfur loading was 1.01–6.20 mg cm^{-2}, in the electrode.

2.5. Preparation of the Li_2S_6 solution

Li_2S and sulfur at a molar ratio of 1:5 were added to an appropriate amount of tetrahydrofuran (THF) by magnetically stirring at room temperature under an argon atmosphere, yielding a burgundy solution.

2.6. Material characterization

The morphology, composition and structure of products were characterized by FE-SEM (SUPARR 55), TEM (JEM-2000EX), HR-TEM (G2 20), XPS (Thermo ESCALAB 250, Al-Kα X-ray source), XRD (Rigaku D/MAX-2400, Cu Kα X-ray source), Raman (DXR), ICP (PerkinElmer Nex ION 300D), Elemental analysis (Vario EL III), TGA (DTG-60AH) and wettability measurement (A SL200B) were conducted to measure the elemental compositon and surface wettability of different samples.

2.7. Electrochemical measurement

For the samples, the samples composites were incorporated into 2025 coin-type cells. The coin-type cells were assembled in a glove box under argon atmosphere (water and oxygen concentration less than 0.1 ppm). For Li-S batteries, it consists of a prepared electrode, polypropylene separator, and lithium foil as the counter electrode. The electrolyte used in this experiment was 1.0 M LiTFSI solution in DOL/DME (1:1 by volume; TFSI = bis(trifluoromethylsulfonyl)imide; DOL = 1,3-dioxalane, DME = dimethyl ether) with 2.0 wt% $LiNO_3$ additive. The amount of electrolyte in a single cell is 45 μL. The galvanostatic charge/discharge tests were carried out on a Land CT2001A battery test system between 1.7 and 2.8 V. The cyclic voltammograms (CV) and Electrochemical Impedance Spectroscopy (EIS) were conducted using a multichannel electrochemical workstation (VMP-300) between 1.7 and 2.8 V at a scan rate of 0.1 mV s^{-1}.

2.8. Density functional theory calculations

Periodic density functional theory (DFT) calculations were carried out by the Vienna ab initio simulation package (VASP) [51,52]. The projector augmented wave (PAW) pseudopotential was adopted to describe the ion-electron interactions [53], and the PW91 gradient-corrected functional [54] was employed in the calculation of the exchange correlation energy. An energy cutoff of 500 eV was used for the plane-wave basis set. Force convergence criterion for atomic relaxation was 0.05 eV/Å. The Brillouin zone was sampled on the basis of the Monkhorst-Pack scheme with a 5 × 5 × 1 k-point mesh [55]. A five-layer slab was used in the calculations. The atoms in the top two

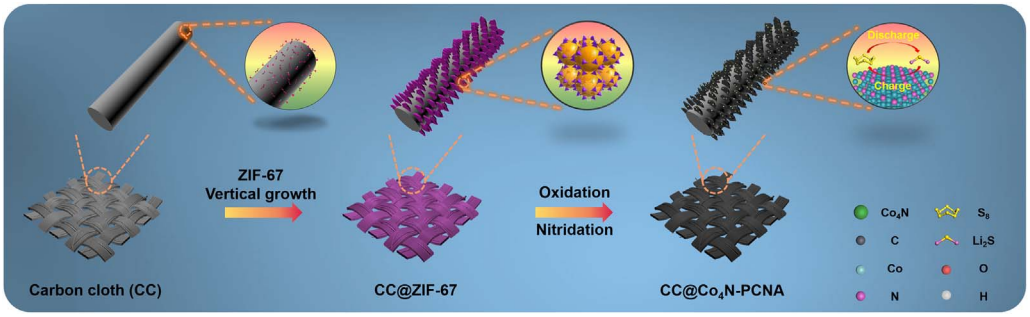

Fig. 1. Schematic illustrations showing the fabrication of CC@Co_4N-PCNA.

layers were fully relaxed and bottom three layers were fixed in their equilibrium positions.

The interaction energy (E_b) between Li_2S_n clusters and Co_4N surface was calculated as follows:

$$E_b = E_{Li_2S_n} + E_{Co_4N} - E_{Li_2S_n+Co_4N} \quad (1)$$

Where $E_{Li_2S_n}$ and E_{Co_4N} represent the total energy of Li_2S_n clusters and Co_4N surface, $E_{Li_2S_n+Co_4N}$ represent the total energy of Li_2S_n-Co_4N complex.

3. Results and discussion

The synthesis strategy for CC@Co_4N-PCNA is schematically illustrated in Fig. 1 and Fig. S1. Firstly, HNO_3-treated carbon cloth was obtained by hydrothermal treatment in a HNO_3 solution. The pretreated conductive CC with well-enriched oxygen-containing functional groups (-OH, -COOH) can provide numerous nucleation sites for ZIFs crystal seed, thus leading to strong bonding force between ZIFs and carbon cloth substrate. Then, the 2D ZIF-67 nanosheet arrays were grown on carbon cloth by mixing a given amount of $Co(NO_3)_2{\cdot}6H_2O$ and 2-methylimidazole (2-MeIm) in aqueous solution at room temperature for 4 h (noted as CC@ZIF-67). The X-ray powder diffraction (XRD) pattern of the as-made CC@ZIF-67 well matches with that of simulated ZIF-67 crystals (Fig. S2). The successful growth of ZIF-67 nanosheet arrays on carbon cloth can be also confirmed by distinct color change from black gray to violet (Fig. S1). Then, the obtained CC@ZIF-67 was finally transformed into CC@Co_4N-PCNA with reserved nanosheet arrays via successive reaction processes in N_2, air and NH_3 atmospheres.

The morphological structure of as-synthesized products was investigated through typical field emission scanning electron microscopy (FE-SEM). Fig. 2a shows the image of ZIF-67 freely grown in the absence of substrate. Obviously, leaf-like nanosheets can be achieved. However, in the presence of CC, ZIF-67 nanosheets are uniformly and vertically grown on the CC substrate (Fig. 2b and Fig. S2d). FE-SEM image of CC@ZIF-67 nanosheets further reveals that the nanosheets possess smooth surfaces (Fig. 2c). Meanwhile, the thickness of the CC@ZIF-67 nanosheets increases with the increase of growth time (Fig S3). After successively annealing the CC@ZIF-67 under N_2 and air atmosphere, Co_3O_4 embedded leaf-like porous carbon nanosheet arrays (noted as CC@Co_3O_4-PCNA) were obtained (Fig. 2d). Nitridation in NH_3 has been demonstrated to be an effective way for preparing specific cobalt nitride [24]. As shown in Fig. 2e-f, the surfaces of nanosheets become rough and porous after treatment under flowing NH_3 at 600 °C. The increase of pores demonstrates that NH_3 can etch the carbon nanosheet arrays to give rise to extra space for hosting substances. It can be also seen that the carbon nanosheets reasonably become thinner (ca. 50 nm) than those in CC@Co_3O_4-PCNA (ca. 65 nm). The Co_4N-PCNA well keeps a 2D nanosheet-shaped structure and distributes on the CC surface in the relatively array form, being similar to leaves grown on branches. For comparison, only calcination of CC@ZIF-67 at 600 °C under an N_2 atmosphere followed by acid etching without oxidation results in the formation of porous carbon nanosheet arrays on carbon cloth (noted as CC@PCNA, Fig. S4) and Co_4N embedded porous carbon nanosheets (Co_4N-PC) were prepared from freely grown ZIF-67 in the absence of CC with the same procedure (Fig. S2).

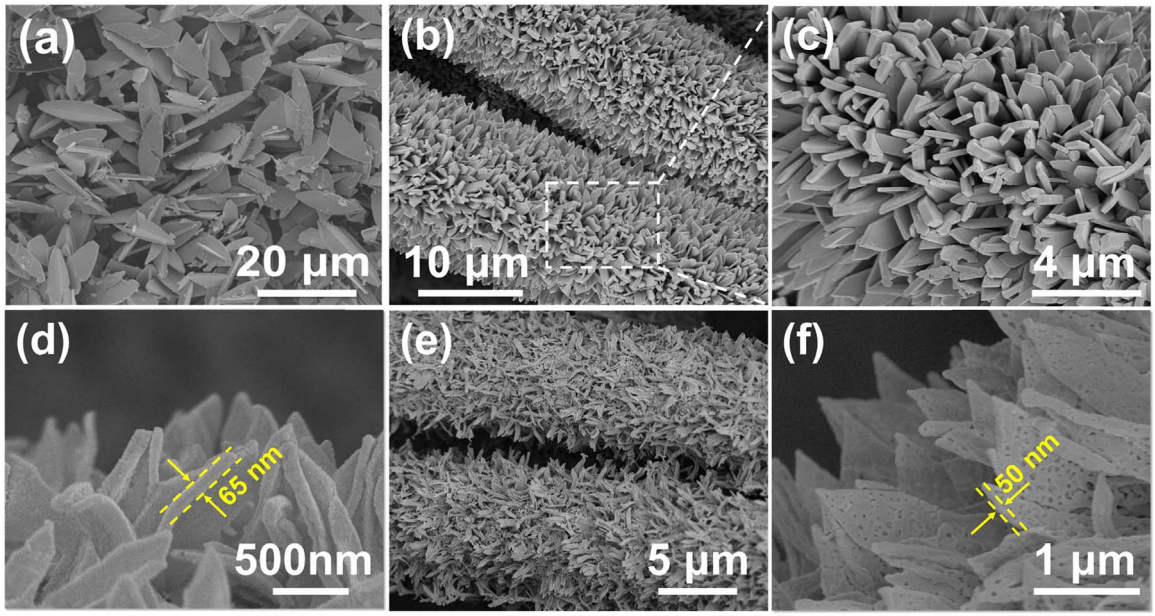

Fig. 2. FE-SEM images of (a) ZIF-67. (b, c) CC@ZIF-67. (d) CC@Co_3O_4-PCNA. (e, f) CC@Co_4N-PCNA.

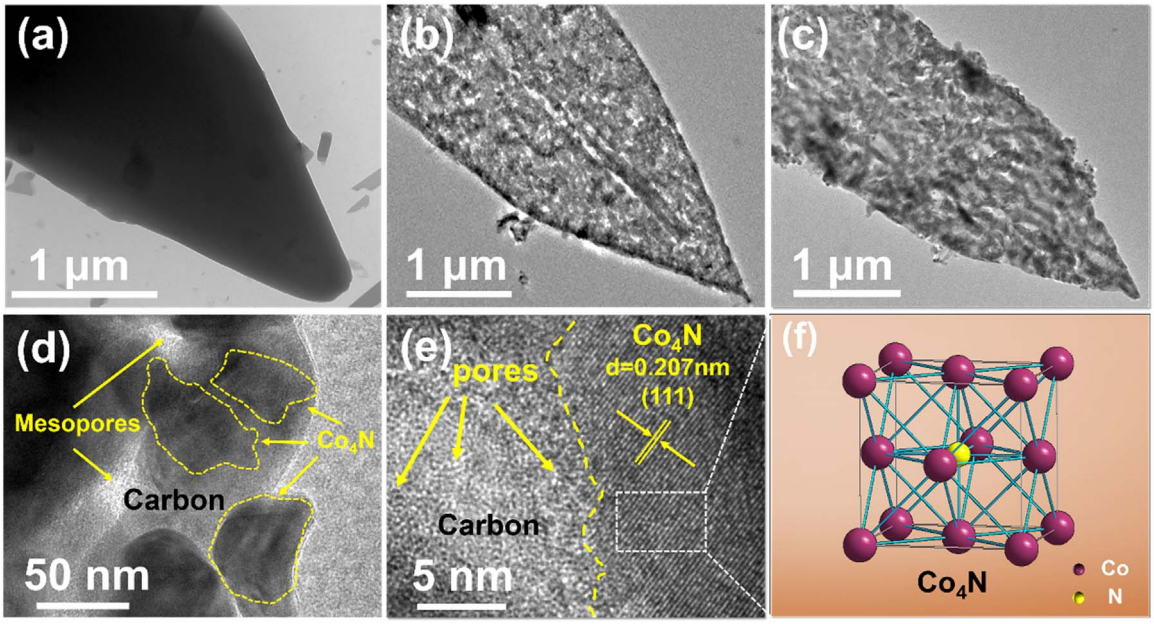

Fig. 3. TEM images of (a) CC@ZIF-67. (b) CC@Co_3O_4-PCNA and (c-d) CC@Co_4N-PCNA. (e) HR-TEM image of CC@Co_4N-PCNA. (f) Unit cell of Co_4N structures.

The structure evolution from CC@ZIF-67 to CC@Co_4N-PCNA was further examined by transmission electron microscope (TEM). The CC@ZIF-67 nanosheet has solid feature with lateral width of 1.5 μm (Fig. 3a). After the conversion via oxidation and nitridation, the leaf-like morphology can be well preserved but a porous structure can be clearly observed (Fig. 3b-c). From a magnified TEM image in Fig. 3d, it can be seen that the surface of the nanostructures is composed of many nanoparticles with the diameters of ca. 40 nm embedded in the porous carbon nanosheets. High-resolution TEM (HR-TEM) images of the nanostructure are shown in Fig. 3e and Fig. S5a, in which the lattice fringes of 0.207 nm and 0.243 nm indexed to the (111) plane of Co_4N and (311) plane of Co_3O_4, respectively, can be observed [21]. The perspective views of the unit cells of Co_3O_4 (space group *Fd3m* (227)) and Co_4N (space group *Pm3m* (221)) are shown in Fig. S5b and Fig. 3f, respectively. Co_4N possesses a similar atomic structure with closely packed cobalt metal, but having longer Co-Co distance due to the N at the center of the unit cell [30].

The XRD patterns of CC, CC@Co_4N-PCNA and CC@Co_3O_4-PCNA are shown in Fig. 4a. The diffraction peak at around 25.6° corresponds to (002) plane of graphitic carbon cloth. The XRD peaks indicate the presence of Co_3O_4 (PDF#42-1467) precursors. Well-defined lattice fringes with a spacing of 0.243 nm, corresponding to the (311) planes of Co_3O_4, are observed (Fig. S5). To obtain CC@Co_4N-PCNA, we carried out the nitridation at 600 °C for 3 h with NH_3 gas flow 50 sccm, the nitridation temperature was optimized via control test. The XRD results (Fig. S6) clearly show the formation of a series of Co-based compounds at different nitridation temperature. The transfer of the Co_3O_4 to Co_4N is based on the following equation [31]:

$$24Co_3O_4+64NH_3 = 18Co_4N + 23N_2+96H_2O \quad (2)$$

As shown in Fig. 4a, after the nitridation process, cubic Co_4N (PDF#41-0943) with (111), (200) and (220) planes appears, which suggests the transformation of Co_3O_4 into Co_4N. In good agreement with XRD results, Fig. 3e shows that the (111) lattice plane corresponds to Co_4N with an interlayer space of 0.207 nm (Fig. 3e). As to the S/CC@Co_4N-PCNA composite, some diffraction peaks of element S at 22.9, 25.7 and 27.6° can be found (Fig. S7a). TEM image shows that sulfur particles are distributed uniformly in porous carbon nanosheet (Fig. S7b), suggesting that sulfur exists well in the Co_4N-PCNA, which renders the composite with the possibility to act as an electrode for LSBs. Quantitative detection by inductively coupled plasma (ICP) and XPS were used to determine the content of each element in various samples (Table S1 and Table S2). Thermogravimetric analysis (TGA) in Figure S7c reveals that the sulfur contents in S/Co_3O_4-PCNA (1.38 mg cm^{-2}) and S/CC@Co_4N-PCNA (1.25 mg cm^{-2} and 6.20 mg cm^{-2}) electrodes are 11.0%, 10.0% and 35.8%, respectively.

Raman spectra of CC, CC@Co_4N-PCNA and CC@Co_4N nanowires (noted as CC@Co_4N NWs, obtained by hydrothermal method [24], for which FE-SEM, TEM images and XRD pattern are shown in Fig. S8) are shown in Fig. 4b, which exhibit two distinct peaks at 1343 and 1601 cm^{-1}, corresponding to the D-band and G-band of carbon materials, respectively. In CC@Co_4N-PCNA and CC@Co_4N NWs, vibration modes of Co elements, such as E_g (480 cm^{-1}), F_{2g} (520 and 617 cm^{-1}) and A_{1g} (688 cm^{-1}), are observed [30]. Moreover, the D- to G-band intensity ratio of CC@Co_4N-PCNA is 1.37, significantly larger than that of CC (1.15), indicating much more defects in the porous carbon nanosheet arrays [32].

X-ray photoelectron spectroscopy (XPS) measurements were performed to investigate the changes of chemical bonding states and elements. The XPS survey spectra reveal that CC@Co_3O_4-PCNA and CC@Co_4N-PCNA are mainly composed of C, Co, N and O elements, where the N content is calculated to be 1.74 at% and 7.73 at%, respectively (Fig. 4c). As shown in Fig. 4d, a new Co peak of CC@Co_4N-PCNA and CC@Co_4N NWs located at near 778.8 eV, corresponding to the binding energy of the Co-N bond [25], is observed after nitridation. It is interesting that compared with CC@Co_4N NWs, CC@Co_4N-PCNA shows an about 0.6 eV positive shift of Co $2p_{3/2}$ and $2p_{1/2}$ peaks in the XPS spectrum. This phenomenon identifies the strong interactions between Co_4N and porous carbon nanosheets [33].

To evaluate the electrochemical performance of the materials, coin cells were assembled with the as-prepared sulfur composites as the cathode material and Li foil as the anode. Profiles obtained by cyclic voltammetry (CV) tests conducted at 0.1 mV s^{-1} are presented in Fig. 5a. The CV of S/CC, S/CC@Co_3O_4-PCNA and S/CC@Co_4N-PCNA exhibit two cathodic peaks and one anodic peak corresponding to the redox reaction of LSBs. Specifically, the peak C2 at 2.30–2.33 V corresponds to the reduction from S_8 to Li_2S_n ($4 \le n \le 8$), while the peak C1 at 2.03–2.05 V is ascribed to the further reduction from Li_2S_n ($4 \le n \le 8$) to Li_2S_2 and eventually to Li_2S. In the following oxidation of cathode, the peak A1 at around 2.37–2.45 V originates from the oxidation of Li_2S to S_8. The Peak C1 of S/CC@Co_4N-PCNA shows a narrower shape, indicating the reaction occurring at this potential is

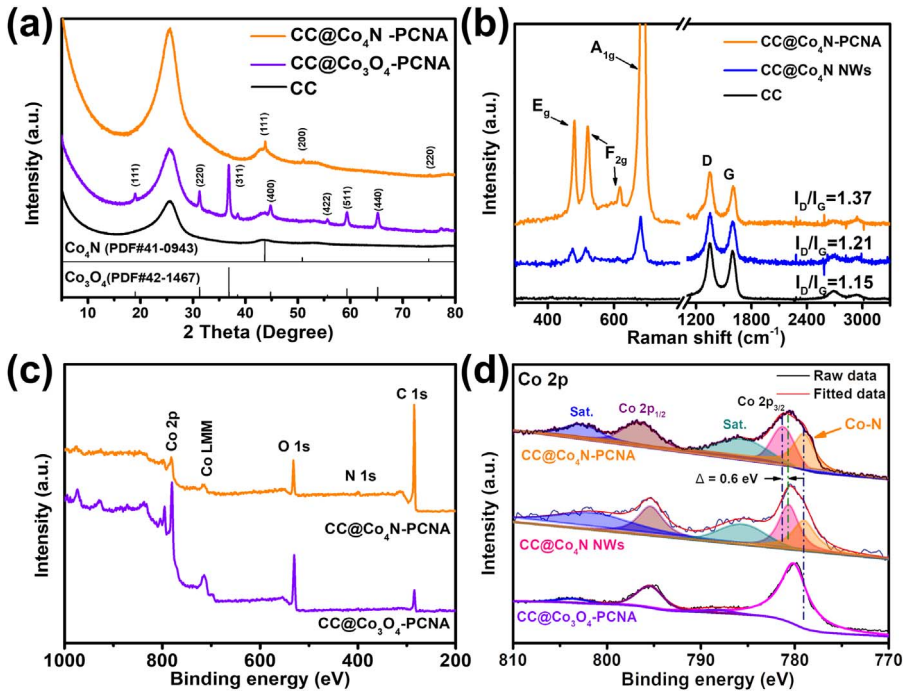

Fig. 4. (a) XRD patterns of CC, CC@Co_3O_4-PCNA and CC@Co_4N-PCNA. (b) Raman spectra of CC, CC@Co_4N NWs and CC@Co_4N-PCNA. (c) XPS full scan. (d) Co 2p XPS spectrum of CC@Co_3O_4-PCNA, CC@Co_4N NWs and CC@Co_4N-PCNA.

greatly enhanced. This means the promoted transformation of soluble LiPSs to Li_2S_2/Li_2S [20]. Meanwhile, the Peak A1 of S/CC@Co_4N-PCNA shifts to a lower potential, suggesting the activation energy is decreased, which accelerates the reaction from Li_2S to S_8. These restrain the possibility for the shuttling of LiPSs. The distance between Peak A1 and Peak C1 0.36 V and 0.42 V the case of S/CC@Co_3O_4-PCNA and S/CC, respectively, while it is 0.32 V for S/CC@Co_4N-PCNA, which implies that polarization is improved because Co_4N is favorable towards lithium-sulfur, in good harmony with the experimental results and previous nitrides studies [22,34]. The positive shift in the cathodic peaks, and the negative shift in the anodic peaks in the S/CC@Co_4N-PCNA electrode clearly reflect the catalytic activity of Co_4N, which promotes the transformation of soluble LiPSs to insoluble products as electro-catalyst used in LSBs [16,35,36].

The galvanostatic discharge and charge curves of S/CC@Co_4N-PCNA cathode between 1.7 V and 2.8 V at 0.5 C and varying current densities from 0.2 to 5 C are shown in Fig. S9. Notably, the curves consist of two discharge plateaus and one charge plateau, which are in good accordance with the CV curves. The plateaus of S/CC@Co_4N-PCNA are flat and stable with a low polarization of 170 mV at 0.5 C, while in the cases of S/CC and S/CC@Co_3O_4-PCNA, a higher voltage hysteresis of 264 and 190 mV, respectively, is observed (Fig. 5b). This may result from the fact that Co_4N embedded into carbon nanosheets catalytically promotes the transformation of insoluble LiPSs to soluble LiPSs in charge-discharge process, as well as increasing the utilization of sulfur in the LSBs [37]. Fig. 5c shows the representative charge-discharge voltage profiles of S/CC@Co_4N-PCNA at a current density of 0.5 C within a cutoff voltage window of 1.7–2.8 V. The S/CC@Co_4N-PCNA cathode delivers initial discharge capacity of 1455 mAh g^{-1} and the capacity still remains 1121 mAh g^{-1} after 100 cycles. Increasing the sulfur loading amount to 6.20 mg cm^{-2}, the S/CC@Co_4N-PCNA cathode still delivers stable cycling performance with a slightly lower discharge 543 mAh g^{-1} at 0.5 C after 200 cycles (Fig. S10). The amount of electrolyte in a cell is 45 μL. The important role of sulfur loading and electrolyte/sulfur ratios (E/S) in shaping the future of Li–S batteries is unambiguously identified [38]. Low E/S (μL: mg): 9:1 for the high sulfur loading. When cycled at current densities of 0.2, 0.5, 1, 2, 3, 4 and 5 C, the corresponding capacities of 1356, 1252, 1076, 936, 859, 802 and 746 mAh g^{-1} can be achieved, respectively. After rapid charge and discharge, a high discharge capacity of 1201 mAh g^{-1} (88.56% of the initial) can be recovered abruptly switching back to 0.2 C, showing the superior structural stability, high porosity and the better conductivity over other materials such as S/CC@PCNA, S/CC@Co_3O_4-PCNA S/CC@Co_4N NWs and S/CC (Fig. 5c). In fact, the high-rate capability of our S/CC@Co_4N-PCNA is superior to most carbon cloth-based cathode previously reported (Fig. S11 and Table S3). Accompanied by rising cobalt prices and limiting cobalt resources, less amount of cobalt is beneficial to the decline in the price of cobalt-based batteries. Hence, the comparisons between the performance and cobalt content of S/CC@Co_4N-PCNA and some cobalt-based cathode lithium-sulfur batteries results have been done (Table S4) [39,40].

The electrochemical impedance spectroscopy (EIS) measurements of fresh cells were conducted to explore their electrochemical dynamics. R_e is the impedance contributed by the resistance of the electrolyte, R_{ct} represents the charge transfer resistance between the electrolyte and sulfur electrode, R_s is the deposit diffusion resistance of SEI film, and CPE arises from double-layer capacitance. Obviously, S/CC@Co_4N-PCNA shows the lowest charge transfer resistance (R_{ct}) among these samples (Fig. S12). Moreover, the wettability and conductivity are also important for its application in electrode material [41]. As shown in Fig. S13, a sharp decrease in contact angle from 120° to 11°, is attributed to the fact that the grown nanosheet arrays can obviously improve the hydrophilicity of the carbon cloth surface [42]. Four probe tests (Fig. S14) show that the conductivity of CC@Co_4N-PCNA (2.59×10^3 S m^{-1}) is higher than that of CC@Co_3O_4-PCNA (1.85×10^3 S m^{-1}) and HNO_3-treated CC (1.53×10^3 S m^{-1}). It is favorable for the fast transport of ion and electrolyte to the surface of the active materials, thus further improving the effective utilization of the electroactive material.

As shown in Fig. 5e, the long-term cycling stability of S/CC@Co_4N-PCNA was further investigated at a current density of 5 C. After the activation process at 0.1 C, the S/CC@Co_4N-PCNA cathode delivers a reversible capacity of 727 mAh g^{-1} and the discharge capacity is stabilized to be 766 mAh g^{-1} at 100th cycle. After 500 cycles, S/CC@Co_4N-PCNA still maintains a discharge capacity of 598 mAh g^{-1}. The capacity decay is only 0.035% per cycle and the Colombic efficiency is

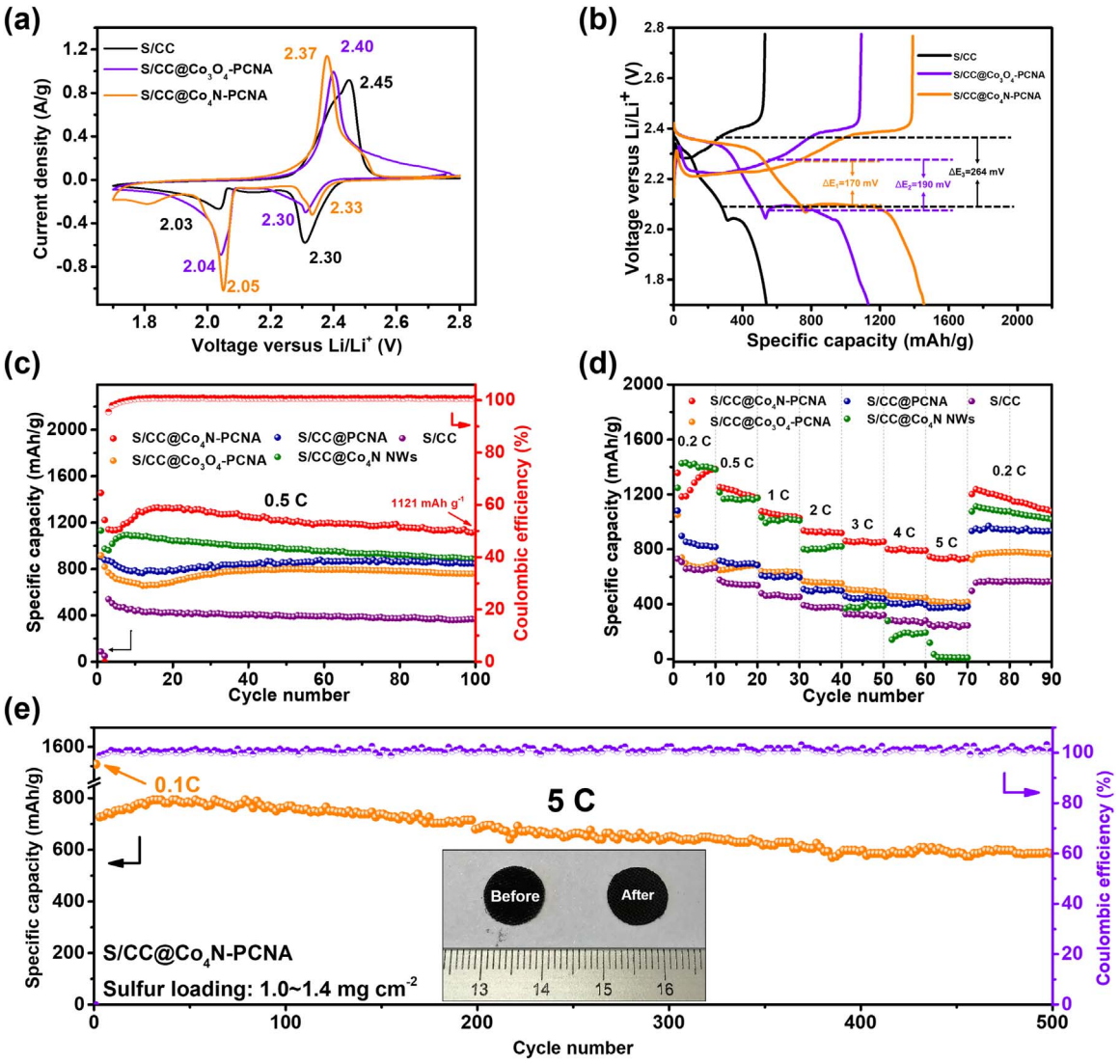

Fig. 5. (a) Cyclic voltammograms curves, (b) Galvanostatic discharge and charge curves of S/CC, S/CC@Co_3O_4-PCNA and S/CC@Co_4N-PCNA at 0.5 C. (c) cycle performance at 0.5 C, (d) rate capability (ranging from 0.2 C to 5 C) of S/CC, S/CC@Co_3O_4-PCNA, S/CC@Co_4N NWs, S/CC@PCNA and S/CC@Co_4N-PCNA. (e) Long-term cycling performance of S/CC@Co_4N-PCNA tested at a high current density of 5 C. The inset in (e) is digital photo of S/CC@Co_4N-PCNA electrodes before and after cycling. The diameters of electrodes are 10 mm.

nearly 100% in charge-discharge process. The leaf-like morphology and 3D braided structure maintain well after the cycling as shown by the digital photo, FE-SEM image, element mapping and XRD patterns (inset of Fig. 5e and Fig. S15), which further proves the toughness of S/CC@Co_4N-PCNA.

To get a deeper insight into the superiority of S/CC@Co_4N-PCNA on restricting the diffusion of LiPSs, density functional theory (DFT) calculations were performed to examine the interaction between sulfur species and Co_4N (Fig. 6a, Fig. S16-17). The (111) planes of Co_4N are chosen as the representative crystalline planes for the simulations owing to their least surface energy and most stable structure. The binding energy between Co_4N nanocrystals and S_8, Li_2S_8, Li_2S_6, Li_2S_4, Li_2S_2, or Li_2S species is -5.33, -7.22, -4.21, -4.18, -6.01 and -4.66 eV, respectively. This indicates that the interaction between the polysulfide species and Co_4N is much stronger than that between Co_3O_4 and LiPSs as previously reported [43,44], and also superior to those of other polar materials [22,45–47]. These DFT calculation results imply that the excellent performance of the S/CC@Co_4N-PCNA originates from the unique surface chemical properties of Co_4N with LiPSs. The polysulfide adsorption abilities of different materials were experimentally and visually compared, as shown in Fig. S18. Obviously, the Li_2S_6 saffron yellow solution becomes more transparent after the addition of CC@Co_4N-PCNA compared with other materials, suggesting its best absorption capability among these materials. The XPS analysis of CC@Co_4N-PCNA composites after the Li_2S_6 adsorption experiment were performed to provide additional evidence for the strong interaction between LiPSs and composites. Upon absorbing the Li_2S_6, the XPS Li 1s of CC@Co_4N-Li_2S_6 shows a strong peak at 55.6 eV (Fig. S19a), which is 0.7 eV shift towards lower binding energy compared with the Li-S of pristine Li_2S_6 (56.3 eV) reported in previous literature [56], the Li-N bond at 56.4 eV assigned to Li in the LiPSs interacting with Co_4N [57]. Meanwhile, the XPS Co 2p spectra of CC@Co_4N-PCNA are shown in Fig. S19b, in which two peaks located at 796.7 and 781.3 eV are attributed to the Co $2p_{1/2}$ and Co $2p_{3/2}$ spin-orbit levels of Co_4N. Upon contacting with Li_2S_6 solution, both peaks shift about 1.0 and 1.1 eV toward lower binding energy and the intensity of the Co-N peak at 778.5 eV decreases [29]. Based on these facts, it can be reasonably concluded that Co_4N have a strong chemical affinity for sulfur and lithium in the LiPSs and the results are also in good agreement with the calculation from DFT.

The superior electrochemical performance of S/CC@Co_4N-PCNA electrode is ascribed to the strong interaction between Co_4N and LiPSs, as well as its facilitated electron/ion transportation and enhanced reaction kinetics. The CV measurements were conducted at different

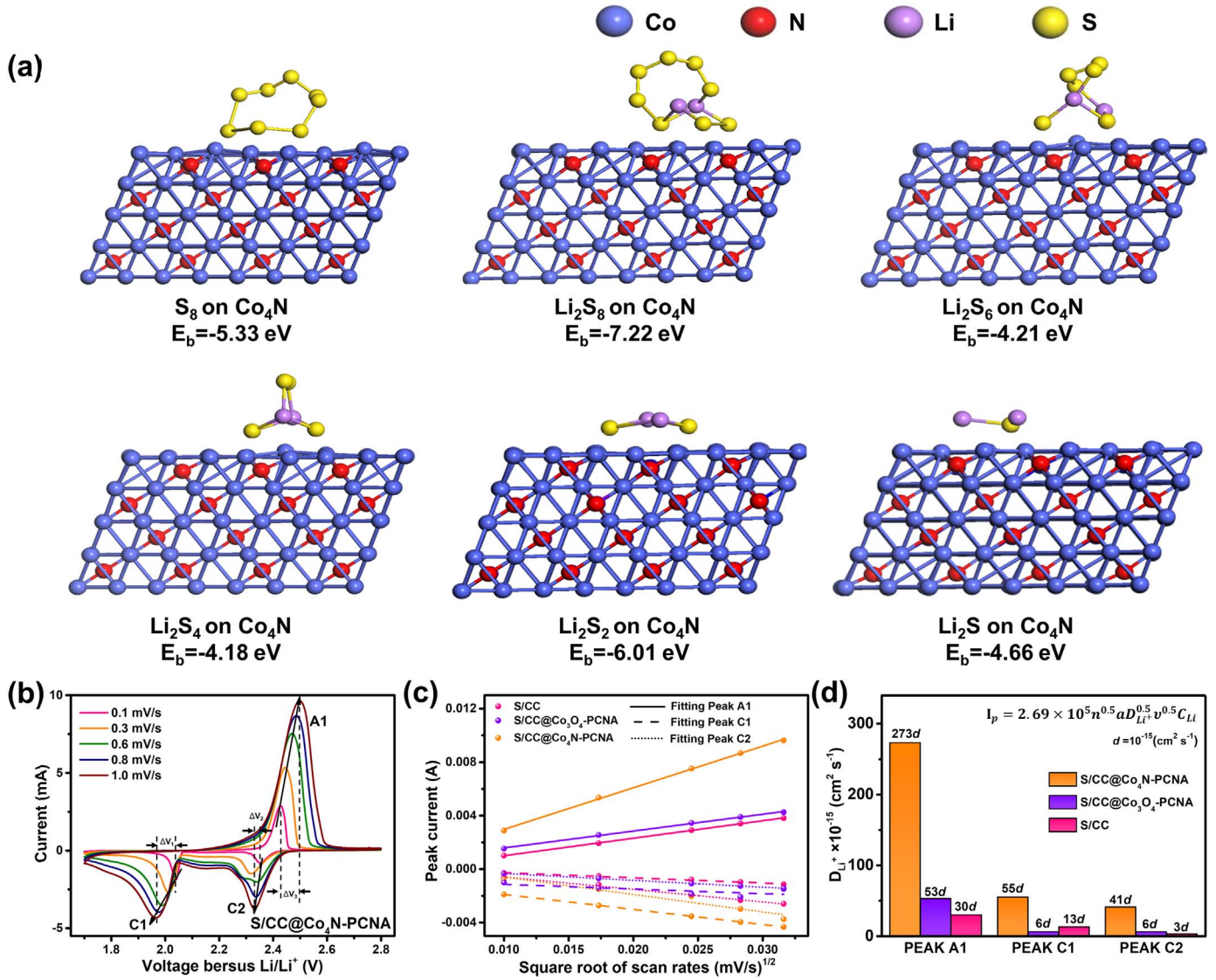

Fig. 6. (a) Calculated interaction energy (E_b) of Li_2S_x (x = 1, 2, 4, 6 or 8) species and S_8 on the (111) planes of Co_4N crystals. (b) Representative voltammograms of S/CC@Co_4N-PCNA cathode obtained at different scan rates. (c) Peak currents versus square root of scan rates of S/CC, S/CC@Co_3O_4-PCNA and S/CC@Co_4N-PCNA. (d) Li^+ diffusion coefficient comparison of the S/CC, S/CC@Co_3O_4-PCNA and S/CC@Co_4N-PCNA cathodes.

scan rates from 0.1 to 1.0 mV s^{-1} to investigate the kinetics of lithium ion insertion/extraction at the electrode interface and lithium-ion diffusion rate in the cell (Fig. 6b, Fig. S20a-b), in which the S/CC, S/CC@Co_3O_4-PCNA and S/CC@Co_4N-PCNA were evaluated within a voltage window of 1.7–2.8 V versus Li/Li^+. It can be obviously shown that distinguishable shift appears with the increase of scan rate owing to the enhanced polarized voltage (ΔV) during fast charge-discharge process. It has been known that the polarization of working electrode leads to the reduction of specific capacitance [23,48], in the case of S/CC@Co_4N-PCNA, it possesses smaller ΔV compared with S/CC@Co_3O_4-PCNA and S/CC, therefore, we can easily understand the reason for its best stability and highest capacity of S/CC@Co_4N-PCNA (Fig. S20c). As shown in Fig. 6c, all anodic and cathodic peak currents keep linear relationship with the square root of scan rates. The lithium diffusion performance can be obtained using the classical Randles-Sevcik equation [49]:

$$I_p = 2.69 \times 10^5 n^{0.5} a D_{Li^+}^{0.5} \upsilon^{0.5} C_{Li} \quad (3)$$

where I_p is the peak currents, n is the number of electrons in the reaction, a is the electrode area, $D_{Li}{}^+$ is the Li^+ diffusion coefficient, υ is the scan rate and $C_{Li}{}^+$ the Li^+ concentration in the electrolyte. The relationship between the slopes of the curves and the corresponding Li^+ diffusion is positive correlation. From the linear relationship of $\upsilon^{1/2}$ and I_p, the Li^+ diffusion coefficient of materials is shown in Fig. 6d. For the S/CC@Co_4N-PCNA cathode, $D_{Li^+}^{A1} = 2.7 \times 10^{-13}$, $D_{Li^+}^{C1} = 5.5 \times 10^{-14}$, and $D_{Li^+}^{C2} = 4.1 \times 10^{-14}$ cm^2 s^{-1} are obtained, which are over 4 times higher than that of S/CC@Co_3O_4-PCNA or S/CC cathode. This phenomenon indicates that the leaf-like S/CC@Co_4N-PCNA allows easy access of liquid electrolytes to the active materials in the porous carbon nanosheets (Fig. S13), thus leading to fast Li-ion diffusion and catalytically promoting the mutual transformation between sulfur and Li_2S_2/Li_2S [15,41].

As illustrated in Fig. 7a-b, the superior electrochemical performance might be attributed to the following reasons. First, the Co_4N embedded in leaf-like porous carbon nanosheet arrays on 3D flexible carbon cloth enables good current collection, which facilitates the transportation of lithium ions and electrons and is beneficial to maintaining the structure integrity. Second, the strong polarity of Co_4N and LiPSs effectively restrains the outward diffusion of poly-

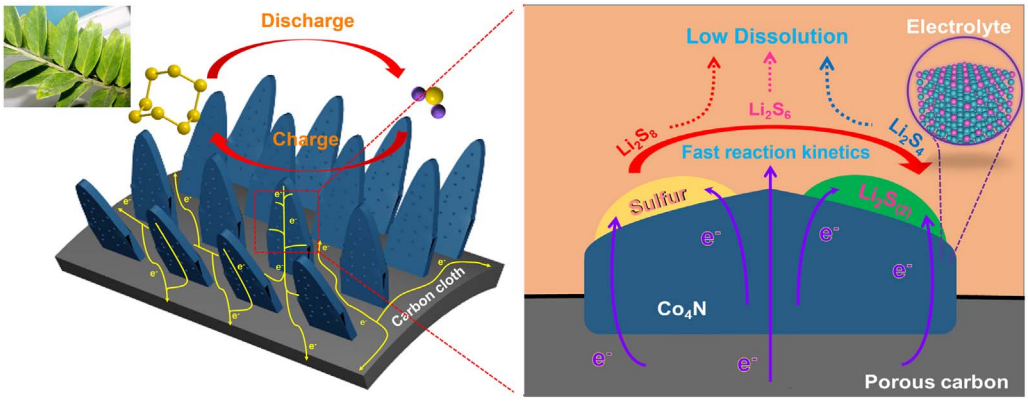

Fig. 7. Schematic illustration of chemical absorption and catalytic effect for polysulfides in the S/CC@Co_4N-PCNA cathode.

sulfide species, reduces the "shuttle effect" of LiPSs in organic liquid electrolytes. Third, the Co_4N with unique catalytic activity propels the formation of Li_2S_2/Li_2S on the cathode, furthermore reducing the diffusion of polysulfide species into the electrolyte. In particular, the high energy density and power density of S/CC@Co_4N-PCNA were obtained to be 285 Wh kg^{-1} and 660 W kg^{-1}, respectively (based on the mass of the cathode electrode, Table S5), and as shown in Fig. S21, the LSBs can light the light-emitting-diode, proving its potential for practical application.

4. Conclusions

In summary, we have designed a novel Co_4N nanoparticles embedded leaf-like porous carbon nanosheet arrays on flexible carbon cloth as a sulfur host for LSBs. This host exhibits excellent conductivity while Co_4N maximizes the effectiveness of moderating LiPSs diffusion and enhances the redox reaction kinetics of polysulfides. Benefiting from the catalytic effect and strong LiPSs adsorption capability of CC@Co_4N-PCNA, the S/CC@Co_4N-PCNA composite cathode shows a high capacity of 1121 mAh g^{-1} at 0.5 C after 100 cycles, an outstanding rate capacity of 746 mAh g^{-1} at 5 C and an ultralow capacity fade rate of 0.035% per cycle over 500 cycles at 5 C. This work opens a new avenue for rational design of metal nitride composite arrays for high performance flexible electrochemical storage and conversion device.

Acknowledgment

This work is supported by the National Natural Science Foundation of China (Grant No. 51672033, U1610105, U1610255), the Open Fund of Key Laboratory of Interface Science and Engineering in Advanced Materials, Ministry of Education, China (KLISEAM 201601), and the Open Sharing Fund Projects for Large Equipment Testing, Dalian University of Technology, China (2016-54).

Appendix A. Supporting information

Supplementary data associated with this article can be found in the online version at doi:10.1016/j.ensm.2018.12.005

References

[1] P.G. Bruce, S.A. Freunberger, L.J. Hardwick, J.M. Tarascon, Li-O_2 and li-s batteries with high energy storage, Nat. Mater. 11 (2011) 19–29.
[2] Z. Wei Seh, W. Li, J.J. Cha, G. Zheng, Y. Yang, M.T. McDowell, P.C. Hsu, Y. Cui, Sulphur-TiO_2 yolk-shell nanoarchitecture with internal void space for long-cycle lithium-sulphur batteries, Nat. Commun. 4 (2013) 1331.
[3] A. Manthiram, S.H. Chung, C. Zu, Lithium-sulfur batteries: progress and prospects, Adv. Mater. 27 (2015) 1980–2006.
[4] A. Manthiram, Y. Fu, S.H. Chung, C. Zu, Y.S. Su, Rechargeable lithium-sulfur batteries, Chem. Rev. 114 (2014) 11751–11787.
[5] J.S. Lee, W. Kim, J. Jang, A. Manthiram, Sulfur-embedded activated multichannel carbon nanofiber composites for long-life, high-rate lithium-sulfur batteries, Adv. Energy Mater. 7 (2017) 1601943.
[6] L. Ji, M. Rao, S. Aloni, L. Wang, E.J. Cairns, Y. Zhang, Porous carbon nanofiber–sulfur composite electrodes for lithium/sulfur cells, Energy Environ. Sci. 4 (2011) 5053.
[7] Z. Li, L. Yuan, Z. Yi, Y. Liu, Y. Xin, Z. Zhang, Y. Huang, A dual coaxial nanocable sulfur composite for high-rate lithium-sulfur batteries, Nanoscale 6 (2014) 1653–1660.
[8] H.J. Peng, T.Z. Hou, Q. Zhang, J.Q. Huang, X.B. Cheng, M.Q. Guo, Z. Yuan, L.Y. He, F. Wei, Strongly coupled interfaces between a heterogeneous carbon host and a sulfur-containing guest for highly stable lithium-sulfur batteries: mechanistic insight into capacity degradation, Adv. Mater. Interfaces 1 (2014) 1400227.
[9] Y. Qiu, W. Li, W. Zhao, G. Li, Y. Hou, M. Liu, L. Zhou, F. Ye, H. Li, Z. Wei, S. Yang, W. Duan, Y. Ye, J. Guo, Y. Zhang, High-rate, ultralong cycle-life lithium/sulfur batteries enabled by nitrogen-doped graphene, Nano Lett. 14 (2014) 4821–4827.
[10] X. Wang, Z. Zhang, Y. Qu, Y. Lai, J. Li, Nitrogen-doped graphene/sulfur composite as cathode material for high capacity lithium–sulfur batteries, J. Power Sources 256 (2014) 361–368.
[11] J. Cao, C. Chen, Q. Zhao, N. Zhang, Q. Lu, X. Wang, Z. Niu, J. Chen, A flexible nanostructured paper of a reduced graphene oxide-sulfur composite for high-performance lithium-sulfur batteries with unconventional configurations, Adv. Mater. 28 (2016) 9629–9636.
[12] H. Xu, Y. Deng, Z. Zhao, H. Xu, X. Qin, G. Chen, The superior cycle and rate performance of a novel sulfur cathode by immobilizing sulfur into porous N-doped carbon microspheres, Chem. Commun. 50 (2014) 10468–10470.
[13] Z.M. Zheng, H.C. Guo, F. Pei, X. Zhang, X.Y. Chen, X.L. Fang, T.H. Wang, N.F. Zheng, High sulfur loading in hierarchical porous carbon rods constructed by vertically oriented porous graphene-like nanosheets for Li-S batteries, Adv. Funct. Mater. 26 (2016) 8952–8959.
[14] F. Pei, T.H. An, J. Zang, X.J. Zhao, X.L. Fang, M.S. Zheng, Q.F. Dong, N.F. Zheng, From hollow carbon spheres to N-doped hollow porous carbon bowls: rational design of hollow carbon host for Li-S batteries, Adv. Energy Mater. 6 (2016) 1502539.
[15] J. He, Y. Chen, A. Manthiram, Vertical Co_9S_8 hollow nanowall arrays grown on a celgard separator as a multifunctional polysulfide barrier for high-performance Li-S batteries, Energy Environ. Sci. 11 (2018) 2560–2568.
[16] H. Xu, A. Manthiram, Hollow cobalt sulfide polyhedra-enabled long-life, high areal-capacity lithium-sulfur batteries, Nano Energy 33 (2017) 124–129.
[17] D. Liu, C. Zhang, G. Zhou, W. Lv, G. Ling, L. Zhi, Q.H. Yang, Catalytic effects in lithium-sulfur batteries: promoted sulfur transformation and reduced shuttle effect, Adv. Sci. 5 (2018) 1700270.
[18] Z. Yuan, H.J. Peng, T.Z. Hou, J.Q. Huang, C.M. Chen, D.W. Wang, X.B. Cheng, F. Wei, Q. Zhang, Powering lithium-sulfur battery performance by propelling polysulfide redox at sulfiphilic hosts, Nano Lett. 16 (2016) 519–527.
[19] H. Lin, L. Yang, X. Jiang, G. Li, T. Zhang, Q. Yao, G.W. Zheng, J.Y. Lee, Electrocatalysis of polysulfide conversion by sulfur-deficient MoS_2 nanoflakes for lithium–sulfur batteries, Energy Environ. Sci. 10 (2017) 1476–1486.
[20] C. Zheng, S. Niu, W. Lv, G. Zhou, J. Li, S. Fan, Y. Deng, Z. Pan, B. Li, F. Kang, Q.-H. Yang, Propelling polysulfides transformation for high-rate and long-life lithium–sulfur batteries, Nano Energy 33 (2017) 306–312.
[21] M. Liu, Q. Li, X. Qin, G. Liang, W. Han, D. Zhou, Y.B. He, B. Li, F. Kang, Suppressing self-discharge and shuttle effect of lithium-sulfur batteries with V_2O_5-decorated carbon nanofiber interlayer, Small 13 (2017) 1602539.
[22] Z. Sun, J. Zhang, L. Yin, G. Hu, R. Fang, H.M. Cheng, F. Li, Conductive porous vanadium nitride/graphene composite as chemical anchor of polysulfides for lithium-sulfur batteries, Nat. Commun. 8 (2017) 14627.
[23] L. Kong, X. Chen, B.Q. Li, H.J. Peng, J.Q. Huang, J. Xie, Q. Zhang, A bifunctional perovskite promoter for polysulfide regulation toward stable lithium-sulfur batteries, Adv. Mater. 30 (2018) 1705219.
[24] P. Chen, K. Xu, Z. Fang, Y. Tong, J. Wu, X. Lu, X. Peng, H. Ding, C. Wu, Y. Xie, Metallic Co_4N porous nanowire arrays activated by surface oxidation as electrocatalysts for the oxygen evolution reaction, Angew. Chem. Int. Ed. 54 (2015) 14710–14714.
[25] Y.Z. Li, T.T. Li, W. Chen, Y.Y. Song, Co_4N nanowires: noble-metal-free peroxidase

mimetic with excellent salt- and temperature-resistant abilities, ACS. Appl. Mater. Interface 9 (2017) 29881–29888.
[26] M.S. Balogun, Y.C. Huang, W.T. Qiu, H. Yang, H.B. Ji, Y.X. Tong, Updates on the development of nanostructured transition metal nitrides for electrochemical energy storage and water splitting, Mater. Today 20 (2017) 425–451.
[27] P.Z. Chen, K. Xu, Y. Tong, X.L. Li, S. Tao, Z.W. Fang, W.S. Chu, X.J. Wu, C.Z. Wu, Cobalt nitrides as a class of metallic electrocatalysts for the oxygen evolution reaction, Inorg. Chem. Front. 3 (2016) 236–242.
[28] L.B. Wang, W.B. Zhang, X.S. Zheng, Y.Z. Chen, W.L. Wu, J.X. Qiu, X.C. Zhao, X. Zhao, Y.Z. Dai, J. Zeng, Incorporating nitrogen atoms into cobalt nanosheets as a strategy to boost catalytic activity toward CO_2 hydrogenation, Nat. Energy 2 (2017) 869–876.
[29] D.R. Deng, F. Xue, Y.J. Jia, J.C. Ye, C.D. Bai, M.S. Zheng, Q.F. Dong, Co_4N nanosheet assembled mesoporous sphere as a matrix for ultrahigh sulfur content lithium-sulfur batteries, ACS Nano 11 (2017) 6031–6039.
[30] K.R. Yoon, K. Shin, J. Park, S.H. Cho, C. Kim, J.W. Jung, J.Y. Cheong, H.R. Byon, H.M. Lee, I.D. Kim, Brush-like cobalt nitride anchored carbon nanofiber membrane: current collector-catalyst integrated cathode for long cycle Li-O_2 batteries, ACS Nano 12 (2018) 128–139.
[31] M.D. Meganathan, S. Mao, T.Z. Huang, G.X. Sun, Reduced graphene oxide intercalated Co_2C or Co_4N nanoparticles as an efficient and durable fuel cell catalyst for oxygen reduction, J. Mater. Chem. A 5 (2017) 2972–2980.
[32] X. Li, Q. Sun, J. Liu, B. Xiao, R. Li, X. Sun, Tunable porous structure of metal organic framework derived carbon and the application in lithium–sulfur batteries, J. Power Sources 302 (2016) 174–179.
[33] W. Guo, C. Yu, S. Li, J. Yang, Z. Liu, C. Zhao, H. Huang, M. Zhang, X. Han, Y. Niu, J. Qiu, High-stacking-density, superior-roughness LDH bridged with vertically aligned graphene for high-performance asymmetric supercapacitors, Small 13 (2017) 1701288.
[34] T. Zhou, W. Lv, J. Li, G. Zhou, Y. Zhao, S. Fan, B. Liu, B. Li, F. Kang, Q.-H. Yang, Twinborn TiO_2–TiN heterostructures enabling smooth trapping–diffusion–conversion of polysulfides towards ultralong life lithium–sulfur batteries, Energy Environ. Sci. 10 (2017) 1694–1703.
[35] W.G. Lim, Y. Mun, A. Cho, C. Jo, S. Lee, J.W. Han, J. Lee, Synergistic effect of molecular-type electrocatalysts with ultrahigh pore volume carbon microspheres for lithium-sulfur batteries, ACS Nano 12 (2018) 6013–6022.
[36] C. Li, Z. Xi, S. Dong, X. Ge, Z. Li, C. Wang, L. Yin, CNTs/MOFs-derived carbon/$Al_2(OH)_{2.76}F_{3.24}$/S cathodes for high-performance lithium-sulfur batteries, Energy Storage Mater. 12 (2018) 341–351.
[37] Y. Dong, S. Zheng, J. Qin, X. Zhao, H. Shi, X. Wang, J. Chen, Z.S. Wu, All-mxene-based integrated electrode constructed by Ti_3C_2 nanoribbon framework host and nanosheet interlayer for high-energy-density Li-S batteries, ACS Nano 12 (2018) 2381–2388.
[38] Z.-W. Zhang, H.-J. Peng, M. Zhao, J.-Q. Huang, Heterogeneous/homogeneous mediators for high-energy-density lithium-sulfur batteries: progress and prospects, Adv. Funct. Mater. 28 (2018) 1707536.
[39] L. Li, L. Zhai, X. Zhang, J. Lu, R. Chen, F. Wu, K. Amine, Recovery of valuable metals from spent lithium-ion batteries by ultrasonic-assisted leaching process, J. Power Sources 262 (2014) 380–385.
[40] M. Hayashi, M. Takahashi, T. Shodai, Preparation and electrochemical properties of pure lithium cobalt oxide films by electron cyclotron resonance sputtering, J. Power Sources 189 (2009) 416–422.
[41] B. Ouyang, Y.Q. Zhang, Y. Wang, Z. Zhang, H.J. Fan, R.S. Rawat, Plasma surface functionalization induces nanostructuring and nitrogen-doping in carbon cloth with enhanced energy storage performance, J. Mater. Chem. A 4 (2016) 17801–17808.
[42] Y. Lu, S. Sathasivam, J. Song, W. Xu, C.J. Carmalt, I.P. Parkin, Water droplets bouncing on superhydrophobic soft porous materials, J. Mater. Chem. A 2 (2014) 12177–12184.
[43] J. Xu, W. Zhang, Y. Chen, H. Fan, D. Su, G. Wang, Mof-derived porous N–Co_3O_4@N-C nanododecahedra wrapped with reduced graphene oxide as a high capacity cathode for lithium–sulfur batteries, J. Mater. Chem. A 6 (2018) 2797–2807.
[44] T. Lei, W. Chen, J. Huang, C. Yan, H. Sun, C. Wang, W. Zhang, Y. Li, J. Xiong, Multi-functional layered WS_2 nanosheets for enhancing the performance of lithium-sulfur batteries, Adv. Energy Mater. 7 (2017) 1601843.
[45] L. Ma, R. Chen, G. Zhu, Y. Hu, Y. Wang, T. Chen, J. Liu, Z. Jin, Cerium oxide nanocrystal embedded bimodal micromesoporous nitrogen-rich carbon nanospheres as effective sulfur host for lithium-sulfur batteries, ACS Nano 11 (2017) 7274–7283.
[46] Q. Pang, D. Kundu, L.F. Nazar, A graphene-like metallic cathode host for long-life and high-loading lithium–sulfur batteries, Mater. Horiz. 3 (2016) 130–136.
[47] Z. Li, J. Zhang, B. Guan, D. Wang, L.M. Liu, X.W. Lou, A sulfur host based on titanium monoxide@carbon hollow spheres for advanced lithium-sulfur batteries, Nat. Commun. 7 (2016) 13065.
[48] T. Lei, Y. Xie, X. Wang, S. Miao, J. Xiong, C. Yan, TiO_2 feather duster as effective polysulfides restrictor for enhanced electrochemical kinetics in lithium-sulfur batteries, Small 13 (2017) 1701013.
[49] X. Tao, J. Wang, C. Liu, H. Wang, H. Yao, G. Zheng, Z.W. Seh, Q. Cai, W. Li, G. Zhou, C. Zu, Y. Cui, Balancing surface adsorption and diffusion of lithium-polysulfides on nonconductive oxides for lithium-sulfur battery design, Nat. Commun. 7 (2016) 11203.
[50] X. Ji, K.T. Lee, L.F. Nazar, A highly ordered nanostructured carbon-sulphur cathode for lithium-sulphur batteries, Nat. Mater. 8 (2009) 500–506.
[51] G. Kresse, J. Hafner, Ab initiomolecular dynamics for open-shell transition metals, Phys. Rev. B 48 (1993) 13115–13118.
[52] G. Kresse, J. Furthmuller, Efficient iterative schemes for ab initio total-energy calculations using a plane-wave basis set, Phys. Rev. B 54 (1996) 11169–11186.
[53] P.E. Blochl, Projector augmented-wave method, Phys. Rev. B 50 (1994) 17953–17979.
[54] J.P. Perdew, Y. Wang, Accurate and simple analytic representation of the electron-gas correlation energy, Phys. Rev. B 45 (1992) 13244–13249.
[55] H.J. Monkhorst, J.D. Pack, Special points for brillouin-zone integrations, Phys. Rev. B 13 (1976) 5188–5192.
[56] G. Zhou, H. Tian, Y. Jin, X. Tao, B. Liu, R. Zhang, Z.W. Seh, D. Zhuo, Y. Liu, J. Sun, J. Zhao, C. Zu, D.S. Wu, Q. Zhang, Y. Cui, Catalytic oxidation of Li_2S on the surface of metal sulfides for Li-S batteries, Proc. Natl. Acad. Sci. USA 114 (2017) 840–845.
[57] J. Xu, W. Zhang, H. Fan, F. Cheng, D. Su, G. Wang, Promoting lithium polysulfide/sulfide redox kinetics by the catalyzing of zinc sulfide for high performance lithium-sulfur battery, Nano Energy 51 (2018) 73–82.